Manuscript
Click here to download Manuscript: HDsEMG_decomposition_rev.doc
Click here to view linked References

A new and fast approach towards sEMG decomposition

Ivan Gligorijević[1], Johannes P. van Dijk[2,3], Bogdan Mijović[1], Sabine Van Huffel[1], Joleen H. Blok[4], Maarten De Vos[1,5]

[1] *Department of Electrical Engineering, SCD-SISTA, KU Leuven, Kasteelpark Arenberg 10, Leuven 3001, Belgium and IBBT Future Health Department.*

[2] *Department of Neurology / Clinical Neurophysiology, Donders Institute for Brain, Cognition and Behavior, Radboud University Nijmegen Medical Centre, PO Box 9101, 6500 HB Nijmegen, The Netherlands.*

[3] *Department of Orthodontics, Center of Dentistry, Ulm University, Medical Centre, Ulm, Germany.*

[4] *Department of Clinical Neurophysiology, Erasmus MC Rotterdam, The Netherlands.*

[5] *Neuroscience Lab, Department of Psychology, Oldenburg University, Germany.*

Corresponding author:

Ivan Gligorijević,

e-mail : ivan.gligorijevic@esat.kuleuven.be

phone: + 32 16 32 96 21

fax: + 32 16 32 19 70

The total number of words of the manuscript, including entire text from title page to figure legends: **6500**

The number of words of the abstract: **207**

The number of figures: **8**

The number of tables: **2**

Abstract:

The decomposition of high-density surface EMG (HD-sEMG) interference patterns into the contribution of motor units is still a challenging task. We introduce a new, fast solution to this problem. The method uses a data-driven approach for selecting a set of electrodes to enable discrimination of present motor unit action potentials (MUAPs). Then, using shapes detected on these channels, the hierarchical clustering algorithm [25] is extended for multichannel data in order to obtain the motor unit action potential (MUAP) signatures. After this first step, more motor unit firings are obtained using the extracted signatures by a novel demixing technique. In this demixing stage, we propose a time-efficient solution for the general convolutive system that models the motor unit firings on the HD-sEMG grid. We constrain this system by using the extracted signatures as prior knowledge and reconstruct the firing patterns in a computationally efficient way. The algorithm performance is successfully verified on simulated data containing up to 20 different MUAP signatures. Moreover, we tested the method on real low-contraction recordings from the lateral vastus leg muscle by comparing the algorithm's output to the results obtained by manual analysis of the data from two independent trained operators. The proposed method showed to perform about equally successful as the operators.

Keywords:

Surface EMG, decomposition, HD-sEMG, motor unit action potential, multichannel, superposition, alignment.

1. INTRODUCTION

Neuromuscular disorders can be roughly divided into neurogenic disorders, which are marked by a loss of functioning neurons, and myogenic diseases, which affect the muscle fibers. Both types have in common that they influence the shape of the action potentials that are generated in a muscle when its motor units (MUs) are activated [6, 11, 28]. These pathophysiological changes tend to be fairly specific for the underlying class of disorders. Therefore, estimating the shapes of the so-called motor unit action potentials (MUAPs) is important for the diagnostic investigation and follow-up of such diseases [6]. Data on the firing patterns of these MUs provide information on the motor control strategies of the central nervous system and, hence, a valuable additional perspective [10].

Recently introduced non-invasive high-density surface electromyography (HD-sEMG) measures the volume-conducted electrical activity from the muscle on the skin overlaying this muscle using a grid of multiple densely spaced electrodes [3, 11]. MUAPs observed on such a grid vary not only between MUs but also from channel to channel. These spatial variations within a MUAP are generally sufficiently characteristic to allow discrimination between them. Therefore, the MUAP recorded with HD-sEMG is sometimes referred to as the "MUAP signature".

When a MU is active, it fires at fairly regular intervals, resulting in a train of repetitive MUAPs. This property supports the assignment of MUAPs to a specific MU. Detecting and classifying each firing of all MUs contributing to a recording is referred to as the full decomposition. To accomplish this, the overlapping mixtures of various MUAPs have to be "demixed".

Several studies aiming at decomposition have been proposed over the past decade (e.g. [7, 12-14, 20, 29-30]). For a review of methods we refer to [25]. However, various problems concerning either automation, processing time, or the number of different MUAP signatures that could be extracted (usually not more than six per recording) remain and ask for new solutions. A more recent, promising approach for full decomposition is the so-called Convolution Kernel Compensation (CKC), reported in [18] and later verified in [19]. Another solution has recently been

reported in [26], which was later used in [8]. However, none of these solutions is freely available for use in the research community.

In this study we introduce a novel approach towards the ultimate aim of full decomposition. Our automated method first extracts MUAP signatures of contributing MUs and then uses these shapes as prior knowledge for subsequent decomposition. In addition, we designed it to be computationally inexpensive, and due to its data-driven nature, it is compatible with multiple surface electrode configurations and equipment. The potential of the method is demonstrated both on simulated and real-life signals.

2. METHODS

2.1 Algorithm

2.1.1 Outline of the algorithm

The algorithm comprises three major steps (see outline in Fig. 1): detection of action potentials (spikes) (which can either be individual MUAPs or mixtures), clustering of similar spikes, and demixing. The goal of clustering is to group similar MUAPs originating from the same active MUs and obtain their mean shapes. The demixing stage provides the time instances (timestamps) at which each MU was active. The output of the algorithm is a set of MUAP signatures and their corresponding firing patterns.

The algorithm exploits the assumption that MUAPs come in trains and have a relatively constant, all-or-none signature on the recording grid. This allows us to cluster similar signatures generated by corresponding active MUs. However, the clustering step leaves many spikes unclustered due to overlapping of MUAPs from different, concurrently active MUs or (less often) appearance of insufficiently large sub-clusters (overclustering) that are not reliable as MUAP representatives. Therefore, in the third step, all of the detected shapes are passed through a demixing process, which assumes that each observation is a superposition of one or more previously obtained shapes and noise. The demixing is performed by minimizing the residue after subtraction of the estimated shapes at proper time lags.

Fig. 1

2.1.2 Detection of spikes

The HD-sEMG array in our setup contains 126 electrodes, which record the signals relative to a far-away reference (i.e., we have monopolar recordings on 126 channels) [3]. Due to densely spaced electrodes, the information content of the signals from adjacent electrodes overlaps to a large extent. This allows using a limited set of electrodes for MUAP detection, one that optimally covers the grid and allows discrimination between different MUAPs. To select these electrodes in a data-driven way, individually suited for each signal, we propose a procedure that automatically detects where repetitive MUAP signatures are maximal. A vector is created by taking the maximal value of all recording channels for each sample. Thereafter, peak detection is performed on this vector to detect possible peak maxima. For each detected peak, the corresponding channel is stored. Channels that contain more than 1% of all detected peaks are used in the spike clustering step. These channels likely include the most prominent peaks of MUAPs. We refer to them as “clustering channels”. Due to the phase shift of MUAPs on different electrodes, the set of clustering channels is over complete – one MU is often expected to contribute more than one channel. For each of the clustering channels, time instances of peaks above the noise level are kept for clustering. This noise level was estimated using the median-based measure introduced in [9].

2.1.3 Clustering of spikes

For each detected spike, samples lying in an interval of ±1.5 milliseconds around the detected peak are stored for each clustering channel. They are consequently concatenated to vectors which are then used as inputs for clustering. Multiple detections are excluded by introducing a detector-dead time (5ms) and treated in the demixing stage (2.1.4). The amount of stored samples represents the empirically determined trade-off between the discriminatory information of the spike and the influence of possible MUAP summation (if multiple MUs are concurrently active).

Clustering of the input vectors corresponding to detected spikes is performed with a multichannel extension of the Wave_clus algorithm [27] as reported in [15]. The

algorithm returns clusters of very similar vectors and a set of nonclustered vectors that appear as outliers. The specific strength of this algorithm lies in the fact that it is unsupervised and that the number of clusters is automatically estimated, i.e. not a priori needed. Its strategy of classification using the nearest neighbor criteria additionally allows for gradual evolving of the shapes of cluster elements.

The algorithm employs hierarchical superparamagnetic clustering (SPC) [2]. SPC was originally used in statistical physics to describe ferromagnetic particle behavior. The input data is modeled as a granular magnet, where each particle is assigned a spin. At very low temperatures, all the spins are aligned (ferromagnetic region). At very high temperatures, all the spins are random (paramagnetic region). There is however, an intermediate, superparamagnetic region; at the right temperature, similar particles will have aligned spins revealing "natural" clusters. Limits of what is considered "natural" are defined by specific application and controlled by tuning of the "temperature" parameter. This parameter determines the depth of differentiation of clustered elements – the line between having too many small clusters and merging elements from different classes. The tuning we employed for sEMG clustering emphasized the need to cluster as many shapes correctly and identify as many possible MUAPs. Another advantage of the clustering method is that also a group of unclustered shapes (usually mixtures of MUAPs) is formed without affecting the remaining clusters. Fig. 2 shows an example of the detected spikes before (Fig. 2 A) and after (Fig. 2 B, C) clustering.

Fig. 2

Once clusters have been identified, a number of the corresponding timestamps is attributed to individual MUs. This number of identified timestamps is dependent on the signal complexity - it usually decreases with higher contraction force. Averaging MUAP shapes (for which the length is predefined by the user) over these attributed timestamps (using median estimator) grants MUAP signatures for each MU. If 2 MUAP signatures exhibit high resemblance (correlation >0.95) they are identified as belonging to the same MU. Additional de-noising of these template MUAP signatures was obtained using the singular value decomposition (SVD) [17]. The SVD was applied on a matrix of MUAP shapes on all channels

stacked below one another. De-noising is achieved by estimating the best rank-5 approximation using the SVD. These signatures will serve for attempted demixing of previously detected spikes. An example of a signature (red) and the associated MUAPs (blue) is shown in Fig. 3.

Fig. 3

2.1.4 Demixing of MUAPs

After clustering, a number of vectors remain unclustered. These include mixtures of MUAPs generated by two or more MUs, additionally corrupted by noise. With the prior knowledge of the obtained MUAP signatures as shown in 2.1.3, these shapes can be demixed by optimizing the fit between the sum of estimated shapes and a detected spike. In order to achieve this, we start from a model of how the activity of MUs is reflected on the recording channels.

Model of HDsEMG recordings

The motor neuron firing sequence can be represented as a pulse train of Dirac functions [18]. The surface EMG recording of active MUs is characterized by how activity from the muscle fibers is reflected on the recording electrodes after propagation through the tissue. This recording ($y_m(\mathrm{k}), m=1...M$, k=1…K, with M channels and K samples), will assume p (p=1..P) possibly active MUs. It can be mathematically expressed (similar to [1]) as the convolution (*) between streams of Dirac impulses (s_p) and their corresponding filters (h_{pm}):

$$\begin{aligned} y_1(k) &= h_{11} * s_1(k) + h_{21} * s_2(k) + \ldots + h_{P1} * s_P(k) + w_1(k) \\ y_2(k) &= h_{12} * s_1(k) + h_{22} * s_2(k) + \ldots + h_{P2} * s_P(k) + w_2(k) \\ &\vdots \\ y_M(k) &= h_{1M} * s_1(k) + h_{2M} * s_2(k) + \ldots + h_{PM} * s_P(k) + w_M(k) \end{aligned} \tag{1}$$

The recording is additionally corrupted by additive noise $w_m(k)$. Each s_p comprises Dirac pulses corresponding to time instances at which the central nervous system triggers the p-th MU (i.e. the MU drive) while the filters h_{pm} account for the p-th MUAP shape recorded on the m-th electrode.

We assume that during the length of the detected spike, each identified MU can be active at most once. Therefore, the activation vectors s_p have non-zero value each time when the MU fires, but can have a non-zero value at maximally one position during the whole length of one detected spike. The goal is, then, to detect the Dirac activations for each MU *p*, knowing the MUAP shapes (h_{pm}) a priori.

Solving the demixing problem

In general, revealing the active MUs and the time positions of the activations during an observed spike is computationally very demanding. It would imply estimating all possible combinations of MUAPs with all possible mutual delays, so that the derived solution corresponds to the observation (recordings). We aim at introducing a simplified algorithm that determines the solution. We start from expressing the convolution relation in a compact matrix representation, by introducing matrices H_{pm}:

$$H_{pm} = \begin{bmatrix} (h_{pm} z_{2L-2}) \\ circshift((h_{pm} z_{2L-2}), 1) \\ \vdots \quad \vdots \quad \vdots \\ circshift((h_{pm} z_{2L-2}), 2L-2) \end{bmatrix} \tag{2}$$

Each row represents a shifted MUAP from the *p*-th MU recorded on the *m*-th channel, h_{pm} denoting this MUAP shape of predefined length L. Here, z_{2L-2} is a zero padding vector of length 2L-2 (denoted in a subscript) allowing to shift shapes, while circshift(X,i) is an operator performing circular shifting to the right of shape X for i samples. Matrices H_{pm} have the size: $(2L-1)\times(L+2L-2)$. All possible delays are accounted for by adding zeros (zero padding) before and after the spike shape (filling in the remaining 2L-2 entries); i.e. if the *p*-th MU is active at position l, then the l-th row of the H_{pm} matrix will model the delay.

We simplify this optimization problem in three ways. First, we perform the optimization only on a selected, discriminative subset of channels. Second, we reduce the complexity of the problem further by using a vectorized concatenation of selected channels. Finally, instead of a simultaneous search for active MUs, we propose an iterative approach. Those steps are explained below.

We propose to reduce the number of channels: each of the P identified MUs will contribute only one channel – the one having the maximal peak of its MUAP signature, resulting in P demixing channels. MUAP shapes from these channels, $h_{p1}, h_{p2}, ...h_{pP}$ are then concatenated separated by zero padding vectors z_{L-1}: $[h_{p1} z_{L-1} h_{p2} z_{L-1} ... z_{L-1} h_{pP}]$. The vector z_{L-1} prevents overlapping of the shapes (2 shapes originating from single MU coming in the same window of length L). These concatenated shapes are shifted in the same fashion as in Eq (2), forming a matrix H_p' for each unit *p*:

$$H_p' = \begin{bmatrix} (h_{p1} z_{L-1} h_{p2} z_{L-1} \dots z_{L-1} h_{pP} z_{2L-2}) \\ circshift((h_{p1} z_{L-1} h_{p2} z_{L-1} \dots z_{L-1} h_{pP} z_{2L-2}), 1) \\ \vdots \qquad\qquad \vdots \qquad\qquad \vdots \\ circshift((h_{p1} z_{L-1} h_{p2} z_{L-1} \dots z_{L-1} h_{pP} z_{2L-2}), 2L-2) \end{bmatrix} \tag{3}$$

This step replaces M matrices in Eq (2) for each unit *p* by a single H_p' matrix, combining the information from all the P demixing channels.

Next, we reduce the recording output of each spike to a single vector. This we refer to as an observation vector (***Ov***). It is – in analogy with the formation of the filter representation Eq (3) - obtained by concatenation of spikes observed on P preselected channels interleaved by zero padding vectors z_{L-1}: $\boldsymbol{Ov} = z_{L-1} y_{p1} z_{L-1} ... z_{L-1} y_{pP} z_{L-1}$ where y_{pi} stands for the i-th channel selected for demixing. These spikes can either belong to a single, or to a mixture of more than one MU. Fitting the introduced model to the recorded data (***Ov***) solves the demixing problem.

The identification of constituting MUAPs is achieved in an iterative way. For each detected MUAP, the observation vector ***Ov*** (in concatenated form) is multiplied with each H_p' matrix resulting into the vectors ($H_p' \cdot (\boldsymbol{O_v})^T$). The matrix H_{p^*}', corresponding to the vector having the maximum entry over all H_p' matrices, is the one corresponding to the most likely unit *p**. The row where this value is found reveals the appropriate delay - non-zero entry of s_p vector in the

original model (1). In case where multiple units are present, the corresponding row of H_{p^*}' of the first identified MUAP is subtracted (peel-off procedure) from the original ***Ov.*** This updated ***Ov*** is used in the next iteration to detect the next most prominent unit. The maximum value of product $H_p' \cdot (\boldsymbol{O_v})^T$ favors the largest shape in a possible mixture in every step, minimizing the errors of subsequent steps.

The noise-level parameter ***Rg*** is defined for the recording as follows:

$$\boldsymbol{Rg} = \sqrt{\sum_{all\ channels} noise_estimate^2 \cdot L} \tag{4}$$

Noise estimate is calculated for each channel as defined in *2.1.2* using the median estimator described in [9]. After each iteration, the sum of RMS of residuals on all channels is calculated. If it is smaller than ***Rg***, it means that the residual is below the noise level, and a successful decomposition has been achieved. For each identified MUAP, timestamp is assigned to corresponding unit's firing pattern if its peak falls in the area ±5ms around the initially detected spike.

The computational process is depicted in Fig 4.

Fig. 4

2.2 Data

2.2.1 Simulated data

The proposed algorithm was validated using MUAP shapes obtained from HD-sEMG recordings of voluntary contractions of the thenar muscles [16]. Recordings were obtained using a flexible surface array of 126 Ag-AgCl electrodes (9 rows and 14 columns) with a diameter of 1.5 mm and the center-to-center electrode distance was 4 mm in both directions [22].

The obtained MUAP shapes with mutual correlation up to 0.95 were kept and used for creation of simulation signals. Firing sequences were simulated to obtain a sEMG interference pattern. The simulated interspike intervals followed a Poisson distribution with mean MU firing rates of 5, 10 or 20Hz. Interference

patterns based on contributions from 3 to 20 active MUs (in increments of 1 MU) were created. For each set of generated spike trains (and template MUAP signatures) this resulted in 18 different signals – the first containing three and the eighteenth containing twenty different MUAP signatures. The duration of the simulated signals was 20 seconds and the sampling frequency was set to 4096 Hz. Four of these sets were created for each mean firing rate (5, 10 or 20Hz).

Additionally, Gaussian noise was added. Realistic noise level was estimated from real recordings of thenar muscles [16] giving an average noise of 5μV root-mean-square (RMS) power. Two levels of noise are used to check the equipment-noise resilience of the algorithm. The first simulation is performed with this estimated, realistic level of noise (5μV). In the second simulation, the noise level of twice this size (10μV) is exploited. The resulting signals were low-pass filtered at 1000 Hz with a fourth order Butterworth filter. Each data set was coupled with each of the noise levels. Signal-to-noise ratio (SNR) was calculated as $20 * \log_{10} \frac{MUAP_{power}}{Noise_{power}}$ (dB). The mean SNR values of MUAP signatures were (15.14±3.03) dB for 5 and (3.31±3.03) dB for 10μV noise level respectively. Overall, 432 signals (2x3x18x4) were used for evaluation of the algorithm.

2.2.2 Real-life data

In addition to the simulation study, we also show the performance of the new algorithm on 20-second long low force voluntary contraction recordings from the lateral vastus leg muscle, an HD-sEMG data set that was previously reported in [21]. In short, eleven healthy volunteers, 6 males and 5 females, aged 20–29 years participated in the study. To obtain a stable interference pattern during an isometric contraction, the subjects were seated with the knee flexed at 90˚ and visual feedback of force was used. Target force was varied between 1% and 10% MVC. In this study, the 5-s long middle sections of recordings have been manually analyzed by two independent, trained operators with the goal of achieving reliable identification of MUs and recovery of their firing patterns. This was possible for 9 subjects (datasets 1-9), with contraction force varying between 1 and 4% MVC. After processing signals from these recordings using our algorithm, the results on these 5-s mid-section intervals were the subject of performance evaluation compared to the operators.

The inter-operator agreement was very high (in 20 out of 25 identified units it was above 95%, the lowest being 63% on a single unit), suggesting that the manually detected firing patterns could be used as a standard for our evaluation.

The main features of the acquisition have been described in detail elsewhere [3, 21]. In short, the electrode array consisted of 10×13 electrodes with center-to-center electrode distance of 5 mm in both directions. Sampling frequency was 2000 Hz and the data were band-pass filtered (3-400Hz). After A/D conversion, a high-pass Butterworth filter of order 6 with cutoff frequency of 10 Hz was used to further reduce the baseline drift.

Because SNR values for the lateral vastus recordings are lower than those of thenar recordings, bipolarly filtered data were used. Bipolar signals were obtained by subtracting the signals from adjacent electrodes in the muscle fiber direction. After the clusters were identified in the bipolar signals, the "maximal peak" channel was selected for each cluster as described earlier (2.1.4), and these sets of channels were used for the demixing process. The noise level was estimated using the method described in [9], being between 5-40 and 0.5-15 μV for monopolar and bipolar representations respectively.

2.3 Validation

To verify the quality of our analysis, temporal and spatial matching parameters were introduced. Temporal parameters, %complete (MUAP train) and precision, defined as in formulae (5) and (6), were used to assess the quality of interference pattern reconstruction.

$$\%complete = \frac{number\ of\ correct\ assignments}{number\ of\ correct\ + number\ of\ missed\ assignments} \tag{5}$$

$$precision = \frac{number\ of\ correct\ assignments}{number\ of\ correct + number\ of\ incorect\ assignments} \tag{6}$$

Tolerance of 5 samples (~1ms) has been taken into account when calculating temporal parameters to account for the effect of noise. Spatial quality, used to describe the reconstruction of MUAP signatures, was estimated using 2

parameters: normalized root mean square error (NRMSE) and correlation coefficient. Each of the signatures obtained by clustering is aligned and compared with the actual shape using these two measures: only if a signature obtained by clustering exhibits a low NRMSE and high correlation at the same time, it can be considered as successfully reconstructed. NRMSE is calculated using formula (7), where $\hat{x}$ represents the estimated shapes obtained by clustering, and x the template (exact) forms. Summation is performed over all samples and channels.

$$NRMSE = \sqrt{\frac{\sum (\hat{x} - x)^2}{\sum x^2}} \tag{7}$$

In case of the simulated signals, exact values for timestamps and template shapes were available. For the real datasets that were used, template MUAP signatures were calculated as the median forms obtained from timestamps grouped in clusters by operators. Similarly, timestamp values marked by the operators were taken as a gold standard for the comparison.

3. RESULTS

3.1 Simulated data

The simulated datasets were decomposed in a fully automatic way. On average, 18 channels (5-25) were used for detection/clustering. Execution time for decomposing a 20 s dataset was between 5 and 15 minutes on an office desktop computer (Intel Core 2 Quad processor at 2.66 GHz with 4 GB of RAM).

The performance of the algorithm showed no statistical difference between the used noise levels (Wilcoxon rank sum test, p=0.78). This came as a consequence of MUAPs being higher above this level for Thenar muscles being close to the skin surface and pointed out that the instrumentation noise is not the main bottleneck of the decomposition attempt. Thus, all the results from signals differing only in the noise level were merged for further analysis. Fig. 5 shows the average percentage of detected and properly classified MUAP signatures for different mean firing rates. Blue, black and red lines represent the mean values while grey areas around the curves indicate the range of all obtained results.

Fig. 5

The %complete and precision of the analysis were evaluated after both the clustering and demixing steps. The sensitivity values as a function of firing frequency and number of active MUs are given in Fig. 6, A-C. Mainly in the case of lower firing rates, %complete sharply increases after demixing. For 5 Hz mean firing rate, %complete reaches average values of 85-95%. However, %complete decreases with the increasing firing rate and the number of present active MUs. At 20 Hz level, the %complete after demixing offers less improvement mainly because not all MUAPs are identified (Fig. 6 C). The precision before and after demixing was in the range of 0.9 to 1 for the 5 Hz mean firing rate. Despite these consistently high values, there was still a difference between the precision before and after demixing. This means that the demixing process decreased the number of wrongly classified units. However, with the increasing firing rate, precision drops and the clustering slightly outperforms demixing. The average values (over all signals containing the MUs with same mean firing rate) for precision across different firing rates (mean±std) are given in Table 1.

Fig. 6

All of the detected MUAPs appearing in large clusters (containing at least 30 elements) were successfully reconstructed. Clustering errors included misclassifications (incorrect assignments) and overclustering (dividing shapes originating from single MU in multiple clusters). While misclassifications were not frequent (indicated by high precision), the algorithm sometimes overclustered the data, leaving up to 3 smaller clusters corresponding to single MU (with correlation between signatures >.95). However, these were successfully merged based on similarity.

The averaged values for the spatial reconstruction parameters (correlation and NRMSE) are also shown in Table 1. As comparison, the mean mutual NRMSE between the MU signatures used for simulation was 1.38±0.53 (range 0.44-5.63). While increasing the number of units had only a marginal effect on these values

(not shown), increasing the mean firing rate decreased the quality of reconstruction.

Table 1

3.2 Real data

In the nine investigated subjects, two trained investigators found 25 reliably identified MUs [21]. Our automated method extracted 24 of these; 1 unit was not detected. Following the described approach, between 7 and 26 electrodes were used for clustering. Fig. 7 shows a typical example of monopolar and bipolar signal representations. In bipolar setting, physiological noise is significantly reduced assisting the decomposition effort.

Fig. 7

Spatial matching between the operator and program extracted shapes was very good, thereby confirming a successful reconstruction of all identified MUAP signatures. Measures of the temporal aspects of the spike trains were mostly good (average %complete and precision > 0.9). Precision and %complete dropped in the presence of very low SNR units (see, e.g., Subject 3) and/or combination of low SNR and similar signatures (e.g. Subject 6, MUs 16 and 18). In all of the cases where attributed firings matched these reported by the operators, the maximal difference was within 3 samples, although the algorithmic tolerance allowed was equal to 5. The performance of our algorithm was compared in detail against the classifications agreed by both operators and the results are summarized in Table 2.

Table 2

To illustrate how well the signatures of the MUAPs after decomposition matched those detected by the operators, Fig. 8 presents both signatures for MU #9 from Table 2, the unit with the lowest correlation value compared to the template (0.83; NRMSE=0.56). The relatively low value is mainly due to noise corruption in the channels where the signature is coming out of noise level. Several additional MUAP trains were also found by our program, but were excluded from the analysis since they were not marked by the operators.

Fig. 8

4. DISCUSSION

In this paper, we presented a new approach aiming at the decomposition of the muscle activity recorded with HD-sEMG. The method is validated on both simulated and real life data. It offers a fast and automated solution for the assessment of both the MUAP signatures of active MUs and their firing patterns. The main novelties of this 3-step HD-sEMG decomposition approach are its automation and computational effectiveness: automated selection of relevant electrodes and detection of timestamps; the "smart" clustering which reliably extracts MUAP signatures; and the demixing by simple multiplication that recovers the firing patterns.

The data-driven selection of clustering electrodes does not guarantee optimality. However, results show that the rationale behind it (electrodes where MUAPs are maximal ease differentiation) picks out electrodes with discriminatory information. Additionally, selecting slightly more electrodes than the number of active MUs ensures spatial distribution information assisting the classification.

The fact that the superparamagnetic clustering algorithm reliably estimates the number of clusters in an unsupervised way, without being impaired by shapes of mixtures of MUAPs, is a strong point. Additionally, it does not assume spherical distance metric. This implies that the mean shapes of cluster components are allowed to slowly evolve in time (forming ellipsoid rather than sphere) – which could help in situations of electrode drifts and slight changes due to MUAP shape instability.

The reliable estimate of MUAP shape in the clustering step, allows then for demixing of (some) MUAP mixtures in order to derive a larger number of timestamps.

Simulated data

The simulated signals were designed to mimic relevant temporal and spatial aspects of the thenar muscles voluntary activity recorded with HD-sEMG. The used SNR values and signal length was similar to other recent studies ([18], [19]). The performance was more affected by the number of active MUs and their mean firing rate than by the noise level. With a mean firing rate of 10 Hz the algorithm on average recovers around 18 of 20 present signatures in the simulation study. Even in the most challenging case, assuming 20 active MUs, all firing at 20 Hz rate, 12-14 signatures could still be reliably extracted.

The grey lines around the indicated mean values in Fig. 5 which represent the borders containing all the obtained results, confirm the stable performance of the described approach. As seen in Table 1, the average spatial reconstruction quality slowly decays with the increasing frequency of spikes. Small decay in signature reconstruction (indicated by increased NRMSE) at higher firing rates can be partially explained by a smaller number of uncorrupted spikes in the clustering phase.

The identified spike timestamps are reliable, as can be seen from the precision values. Precision values are higher in the demixing step compared to clustering for firing frequency of 5 Hz, however, this ratio changes slightly in favor of clustering at 10 and 20 Hz rate. It can happen in the demixing step, that a wrong unit is peeled off when a MU signature was not identified in the clustering step and a similar shape was assigned instead. The %complete drops mainly due to the increased firing rate. It reaches the average values of ~35, 65 and 82% for mean firing rates of 20, 10 and 5 Hz respectively. Only more validation studies with real signals can tell how severe the drop in %complete is at higher contraction. A high firing rate affects the number of identified signatures: each missing shape implies that the mixtures containing this shape and any other MUAP cannot be resolved. When the majority of signatures is successfully recovered, like in the case of mean firing rate of 5 Hz or 10 Hz, %complete is only slowly decaying with increasing number of active MUs.

Real data

We also demonstrated the performance of the new method on a set of manually scored recordings from the lateral vastus leg muscle. These datasets are, despite the low contraction force, challenging because observed MUAPs have very low SNR compared to those of the thenar muscles as used in the simulations. Part of the present noise stems from physiological sources such as activity from deep MUs or distant muscles. To reduce the effect of this physiological noise, bipolar spatial filtering was applied prior to the processing.

Out of the 25 different MUAP signatures detected by the two operators in the recorded data, 24 were identified with our automated approach. Our method for selecting the clustering electrodes did not identify the appropriate electrode in the case of the missed unit, due to the dominance of two spread-out units. Possibly, having better way to choose clustering channels would enable detection of this unidentified unit. The relative number of clustering electrodes with respect to the number of existing MUPTs was higher than in simulated signals. This came as a result of a larger shift of spikes between distant channels than in case of the thenar muscles.

The results of the real signals largely confirm the findings of the simulation study. The %complete achieved by our algorithm (median value 91%) is similar to the level reported in other state of the art HD-sEMG decomposition studies [7, 19]. Since the signals corresponded to low contraction forces, and the fact that the operators decided that the firing patterns were successfully reconstructed, the %complete values can be considered close to ones that would be obtained when comparing with the ideal, complete firing patterns. The situation where a firing was marked by the operators and not by our program, can be explained by three different reasons. First, when many (similar or small) unidentifiable MUAPs were present, the algorithm was not able to decompose the mixtures containing unrecognized shapes; second, more substantial differences in MUAP shapes induced by noise (e.g. datasets 1 and 9); and third, similar shapes can cause wrong assignments (e.g. in dataset 6). Nevertheless, the firing patterns could still be reliably enough approximated to derive the dominant mean firing frequency of the identified units. It is also worth mentioning that our algorithm identified several

additional units. These had not been detected by the operators and were, therefore, excluded from evaluation.

In accordance with these results, the next step appears to be further validation of our algorithm by means of co-registration and correlation of intramuscular and surface EMG recordings as performed in [7, 19]. It can be anticipated that in clinical settings, unstable contractions and physiological noise can impede the extraction of all present signatures and hence also the quality of firing pattern reconstruction can go down. The key assumptions for our algorithm are that each MUAP has a relatively stable shape and appears a number of times to be recognized as a cluster. The former is inherently shared by most of automated methods and although the clustering method we used can deal with certain shape instability, it is yet to be explored to which extent it is resilient to such cases. The latter assumes having a number of uncorrupted shapes suggesting a limitation connected with high contractions and needs to be explored further.

To achieve decomposition in a wider range of applications, the demixing strategy could be extended. As an initial demixing algorithm, we opted for a straight-forward but reliable solution for demixing, allowing only known shapes to participate in mixtures. Despite the fact that MUAP shapes are in general reliably estimated, %complete should be further improved in cases where not all present units are detected in the clustering step. By modifying the demixing criteria to observe the residue on only a part of the grid associated with the identified MUAP shape could be an obvious step to detect more timestamps.

Another way to extract more timestamps is by allowing resolution of cases of phase cancellation between nearly simultaneous MUAPs (e.g., similar to previous work on intramuscular EMG decomposition [24]) at a higher computational cost. The idea would be to estimate all possible mixture shapes in advance by exploring all possible combinations. A possible way to extract additional MUAP signatures, is to employ approaches using e.g. convolutive constrained ICA ([4]) where a mixture is described as a sum of known and yet unidentified sources which are then extracted.

ACKNOWLEDGEMENTS

We acknowledge financial support from: GOA MaNet, PFV/10/002 (OPTEC), FWO project G.0427.10N (Integrated EEG-fMRI), IUAP P6/04 (DYSCO); IMEC SLT PhD Scholarship; M. De Vos obtained a Von Humboldt stipend.

REFERENCES

[1] Abed-Meraim K, Q Wanzhi, Hua Y (1997) Blind system identification. P IEEE, 85(8):1310-1322

[2] Blatt, M, S Wiseman, E Domany (1996) Superparamagnetic clustering of data. Phys Rev Lett, 76: 3251–3254

[3] Blok JH, JP van Dijk, G Drost, MJ Zwarts et al (2002) A high-density multichannel surface electromyography system for the characterization of single motor units. Rev Sci Instrum 73(4):1887-1898

[4] Castella M, Bianchi P, Chevreuil A et al (2006) A blind source separation framework for detecting CPM sources mixed by a convolutive MIMO filter. Signal Processing 86(8):1950-1967

[5] Daube JR, Rubin DI (2009) Needle electromyography. Muscle Nerve 39(2):244-70

[6] Denny-Brown D (1949) Interpretation of the electromyogram. Arch Neurol Psychiatry, 61:99–128

[7] De Luca CJ, A Adam, R Wotiz et al (2006) Decomposition of Surface EMG Signals. J Neurophysiol 96:1646-1657

[8] De Luca CJ, EC Hostage (2010) Relationship Between firing rate and recruitment threshold of motoneurons in voluntary isometric contractions. J Neurophysiol 104(2):1034-1046

[9] Donoho DL and JM Johnstone (1994) Ideal spatial adaptation by wavelet shrinkage. Biometrika. 81(3):425-455

[10] Dorfman LJ, JE Howard and K. C. McGill (1989) Motor unit firing rates and firing rate variability in the detection of neuromuscular disorders. Electroen Clin Neuro 73(2):215-224

[11] Drost G, DF Stegeman, BGM Van Engelen et al (2006) Clinical applications of high-density surface EMG: A systematic review. J Electromyography Kinesiol 16:586-602

[12] Florestal JR, PA Mathieu, A Malanda (2006) Automated decomposition of intramuscular electromyographic signals. IEEE T Bio-Med Eng 53(5):832-839

[13] Florestal JR, PA Mathieu, KC McGill (2009) Automatic decomposition of multichannel intramuscular EMG signals. J Electromyography Kinesiol 19:1-9

[14] Gazzoni M, D Farina, R Merletti (2004) A new method for the extraction and classification of single motor unit action potentials from surface EMG signals. J Neurosci Methods 136(2):165-177

[15] Gligorijević I, M De Vos, JH Blok et al (2011) Automated way to obtain motor units' signatures and estimate their firing patterns during voluntary contractions using HD-sEMG. Conf Proc IEEE Eng Med Biol Soc. 4090-4093

[16] Gligorijević I, BTHM Sleutjes, M De Vos et al (2012) Correcting electrode displacement errors in motor unit tracking using high density surface electromyography (HDsEMG). In Proc. of the 7th International Workshop on Biosignal Interpretation (BSI2012), Como, Italy

[17] Golub, GH, Van Loan CF. (1996), Matrix Computations, 3rd ed., Johns Hopkins University Press

[18] Holobar A, D Zazula (2007) Multichannel blind source separation using convolution kernel compensation. IEEE Trans Signal Process 55(9):4487-4496

[19] Holobar A, MA Minetto, A Botter et al (2010) Experimental analysis of accuracy in the identification of motor unit spike trains from high-density surface EMG. IEEE Trans Neural Syst Rehabil Eng 18(3):221-229

[20] Kleine BU, JP van Dijk, BG Lapatki et al (2007) Using two-dimensional spatial information in decomposition of surface EMG signals. J Electromyography Kinesiol 17:535–548

[21] Kleine BU, JP van Dijk, MJ Zwarts et al (2008) Inter-operator agreement in decomposition of motor unit firings from high-density surface EMG. J Electromyography Kinesiol 18:652–661

[22] Lapatki BG, JP van Dijk, IE Jonas et al (2004) A thin, flexible multielectrode grid for high-density surface EMG. J Appl Physiol 96(1):1327-336

[23] Maathuis EM, J Drenthen, JP van Dijk et al (2008) Motor unit tracking with high-density surface EMG. J Electromyography Kinesiol 18:920-930

[24] McGill KC (2002) Optimal resolution of superimposed action potentials. IEEE T Bio-Med Eng 49(7):640-650

[25] Merletti R, A Holobar, D Farina (2008) Analysis of motor units with high-density surface electromyography. J Electromyography Kinesiol 18:879-890

[26] Nawab SH, SS Chang, CJ De Luca (2010) High-yield decomposition of surface EMG signals. J Clin Neurophysiol 121(10):1602-1615

[27] Quian Quiroga R, Z Nadasdy, Y Ben-Shaul (2004) Unsupervised spike detection and sorting with wavelets and superparamagnetic clustering. Neural Computation 16:1661-1687

[28] Roeveld K, DF Stegeman, B Falck et al (1997) Motor unit size estimation: confrontation of surface EMG with macro EMG. J Electroen Clin Neuro 105:181-188

[29] Xu Z, S Xiao, Z Chi (2001) ART2 Neural Network for Surface EMG Decomposition. Neural Comput Appl 10(1):29-38

[30] Zazula D, A Holobar (2005) An approach to surface EMG decomposition based on higher-order cumulants. Comput Meth Prog Bio 80(1):51-60

FIGURE CAPTIONS

Fig. 1: Schematic outline of the algorithm. Three major steps can be recognized: 1) spike detection, 2) clustering of spikes and extraction of MUAP signatures, 3) demixing superpositions and the recovery of interference pattern by using the MUAP signatures obtained in step 2

Fig. 2: Example of clustering. (A) Overlapped and aligned input vectors based on concatenated spikes from 19 clustering channels. (B) and (C) Clustering places the detected spikes accurately into two distinct groups with small intragroup variability. The vector data in (B) can therefore be assigned reliably to a different MU than those in (C)

Fig. 3: An example of overlaid MUAPs belonging to the same MU (blue) together with the median shape in red (signature). Median shape is unaffected by a single misclassified MUAP (also visible); Clustering electrodes are marked in grey

Fig. 4: Toy example of demixing algorithm; A) Each identified MUAP signature contributes one electrode for demixing (marked using red, blue and green colors); B) Filter matrices (H_{pm}) corresponding to *p*-th MUAP shape recorded on *m*-th electrode are combined into a single H_p' matrix for representing the *p*-th MU using concatenations of P demixing channels separated by zero padding; C) For each detected spike, observation vector (***Ov***) is created from raw signals by concatenation of spikes on demixing channels; thereafter, the most likely candidate MUAP is identified by the maximum of the products of all H_p' matrices and transposed ***Ov***; this maximum reveals the first MUAP (*p**) to be peeled off while the position of this maximum (i) reveals adequate shape delay (row of the H_{p*}' matrix); D) ***Ov*** vector is modified (***Ov***(1)) by subtraction of identified row of H_{p*}' matrix from ***Ov*** and the next iteration is performed; once the residue falls below the noise level, a successful decomposition is obtained and the next timestamp is subjected to the demixing process.

Fig. 5: Mean percentage of reconstructed MUAP trains (MUPTs) as a function of mean firing rate and the number of present active MUPTs; mean values are shown in blue, black and red colors (for 5, 10 and 20 Hz mean firing rates) while all the obtained results are contained within the grey areas.

Fig. 6: Effect of (additional) demixing on the %complete of identified MUs' trains for 5, 10 and 20 Hz mean firing rate as a function of number of present active MUPTs (A-C respectively). Mean values are shown in red (demixing) and blue (clustering). Grey areas around the mean values portray the standard deviation.

Fig. 7: Monopolar (A) and bipolar (B) view of signal (~180ms; dataset 5); MUAPs (1,2 and 3) are indicated in different colors (B); very similar spikes (2 and 3) were successfully identified as separate MUAPs; unidentified small MUAPs are marked in grey, i.e. physiological noise; corrupted electrodes were switched off (zero values)

Fig. 8: The MUAP with the lowest spatial correlation (0.83; NRMSE=0.56; MU #9 in Table 2) between the actual (blue) and recovered (red) signatures. The expanded, lower figure zooms in on the part of the array that is closest to the MUs neuromuscular junction (has the largest signals). This example illustrates that even in the cases with a relatively low correlation, the reconstructed and original shapes match very well. The low correlation value is primarily due to the very small signal size in most channels in combination with the influence of noise

TABLES

	Mean firing rate		
	5 Hz	10 Hz	20 Hz
Correlation	0.99±0.01	0.98±0.02	0.94±0.04
NRMSE	0.06±0.03	0.19±0.10	0.40±0.17
Precision clustering	0.94±0.04	0.93±0.04	0.87±0.04
Precision demixing	0.96±0.04	0.91±0.05	0.82±0.05

Table 1:Average (over all signals of MUs with same firing rate) quality of spatial reconstruction for different mean firing rates (mean ± standard deviation) expressed as Pearson correlation coefficient and the normalized root mean square error (NRMSE). Values of precision after clustering and demixing procedures are also portrayed.

MU	Subject	Force (%MVC)	SNR (dB)	Firings		Temporal		Spatial	
				Program	Operators	%complete	Precision	Correlation	NRMSE
1	1	1	-7.86	39	47	0.83	0.94	0.94	0.48
2	1	1	-5.37	38	45	0.84	0.90	0.90	0.36
3	1	1	-3.56	21	25	0.84	1.00	0.95	0.39
4	1	1	-3.80	26	30	0.87	0.95	0.94	0.45
5	1	1	3.53	47	49	0.96	1.00	0.99	0.12
6	1	1	-1.41	19	25	0.73	0.89	0.95	0.27
7	2	1	-3.56	53	42	1.00	0.92	0.95	0.21
8	2	1	-2.86	30	38	0.79	1.00	0.85	0.42
9	2	1	-6.47	45	42	0.90	0.85	0.83	0.56
10	3	1	-10.60	31	35	0.86	0.97	0.97	0.24
11	4	2	-8.19	43	46	0.91	0.98	0.99	0.10
12	4	2	12.26	28	27	1.00	0.96	0.95	0.23
13	5	1	-3.46	32	31	0.94	0.91	0.97	0.23
14	5	1	-3.59	39	39	0.95	0.95	0.97	0.21
15	5	1	2.11	51	51	1.00	1.00	0.98	0.12
16	6	1	-4.58	43	24	0.67	0.37	0.93	0.39
17	6	1	-4.09	24	23	0.96	0.92	0.96	0.38
18	6	1	-2.24	41	40	0.85	0.83	0.98	0.20
19	6	1	11.76	35	35	1.00	1.00	0.97	0.29
20	7	1	-4.04	32	35	0.86	0.94	0.84	0.36
21	7	1	-4.41	*	40	*	*	*	*
22	7	1	0.47	38	41	0.93	1.00	0.89	0.23
23	8	4	3.01	49	45	0.96	0.88	0.98	0.22
24	9	1	-3.79	31	40	0.78	1.00	0.92	0.29
25	9	1	-3.47	49	49	1.00	1.00	0.96	0.27

* - unit was not found using the program

Table 2: Comparison of automatic decomposition program and the operators; each of the MUs indicated by the operators was compared in terms of the quality of reconstructed MUAP signatures and the associated firing patterns.

Figure 1
Click here to download Figure: Fig1.eps

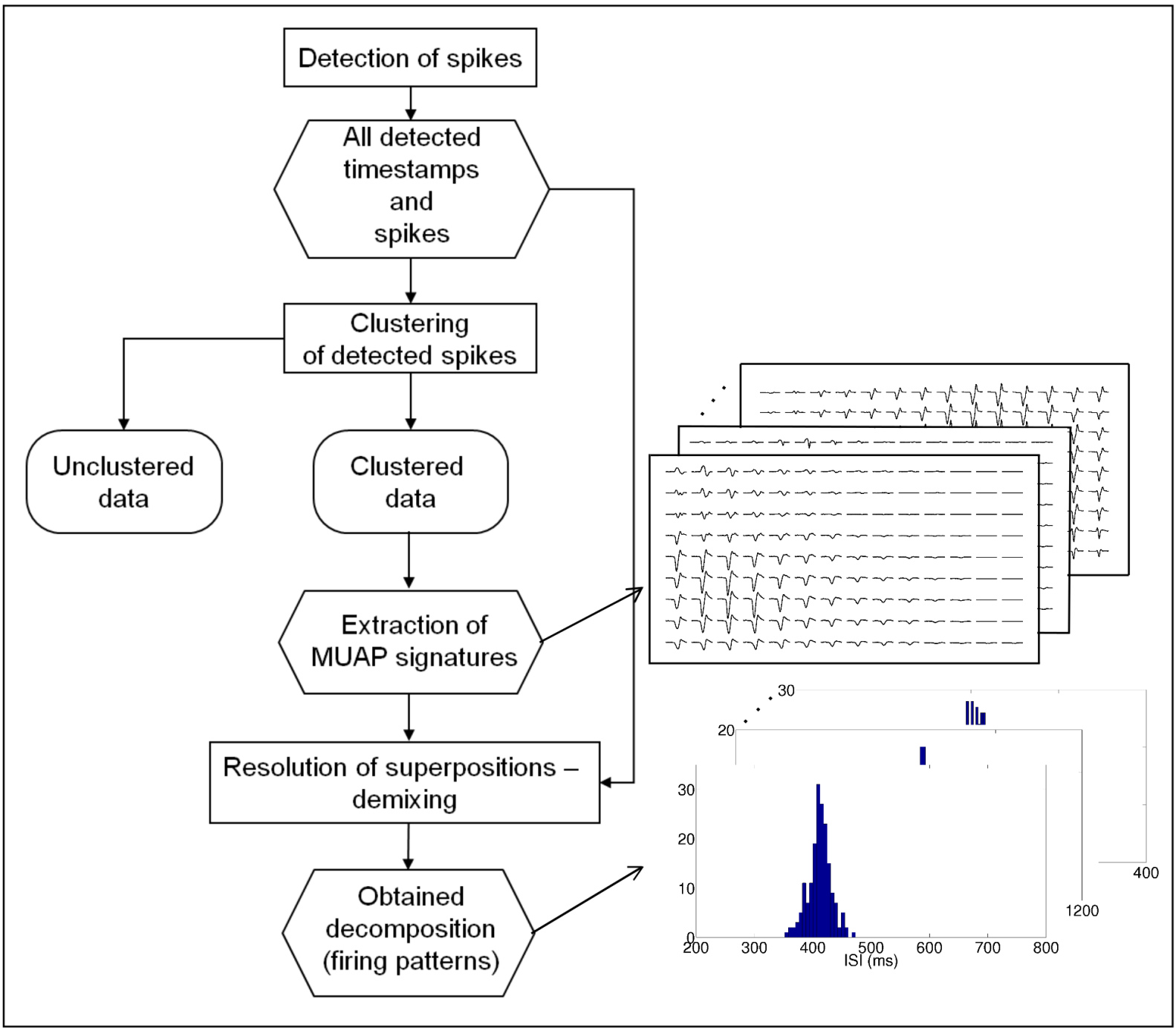


Figure 2
Click here to download Figure: Fig2.eps

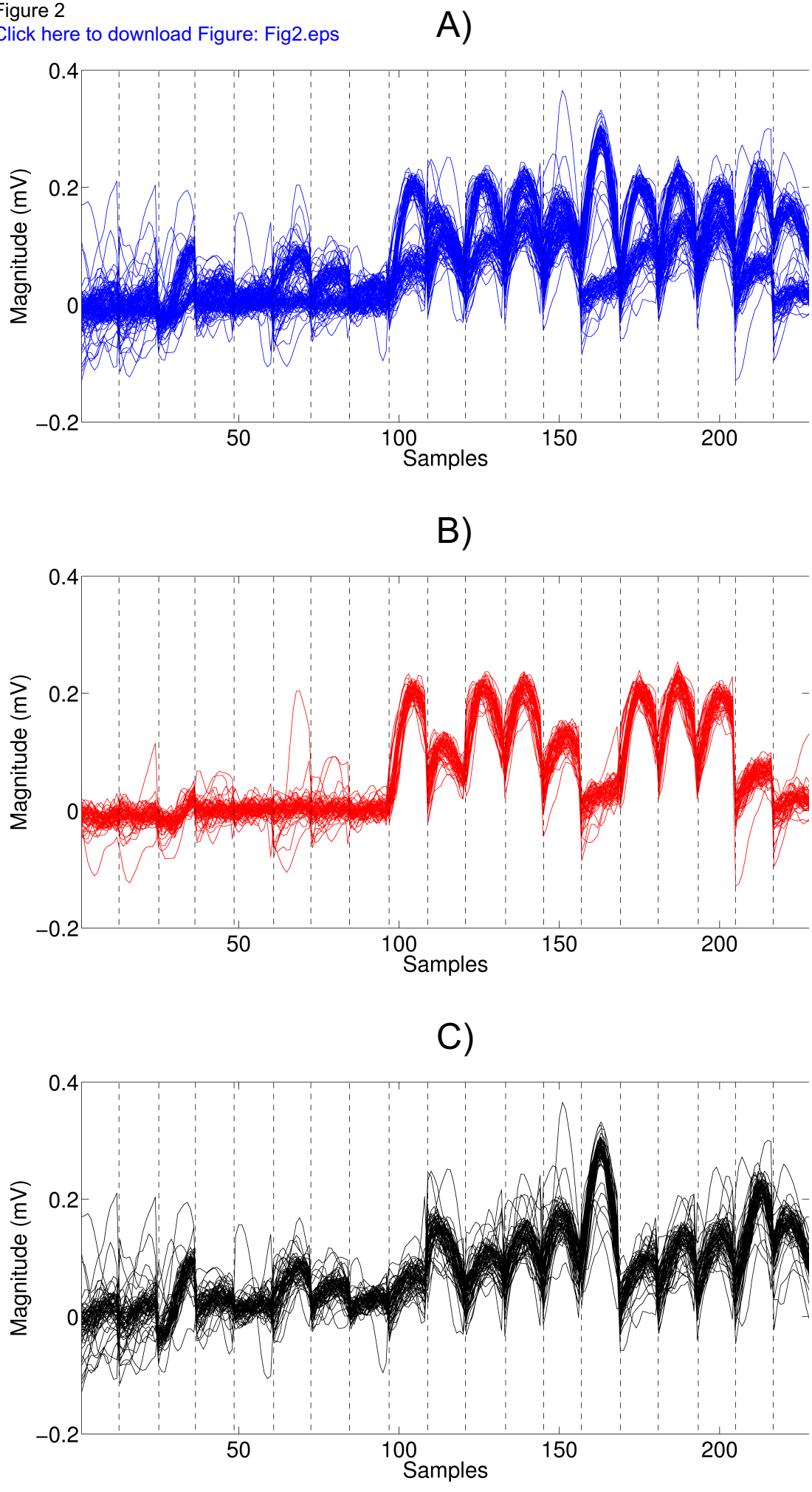


Figure 3
Click here to download Figure: Fig3.eps

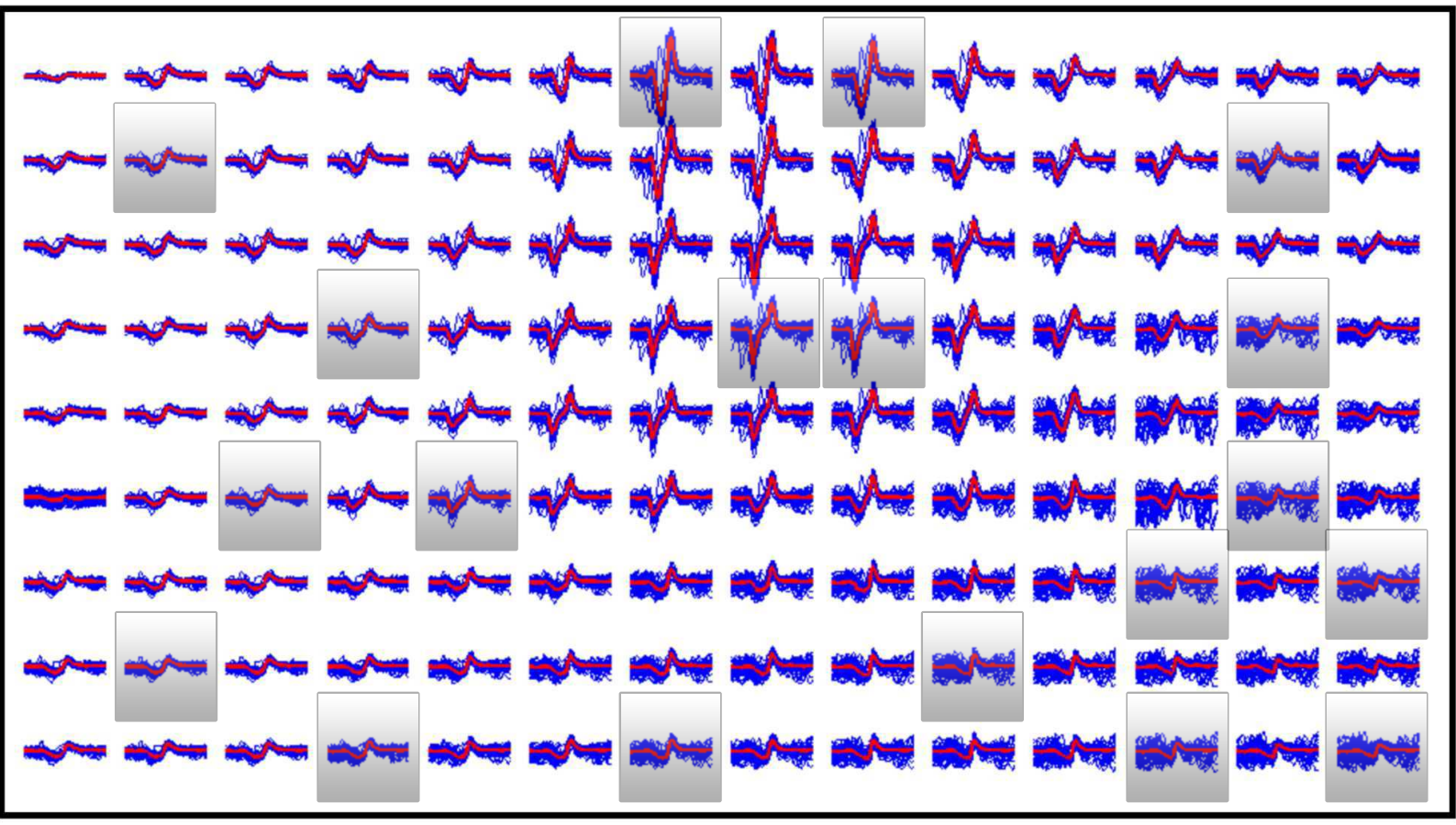


Figure 4
Click here to download Figure: Fig4.eps

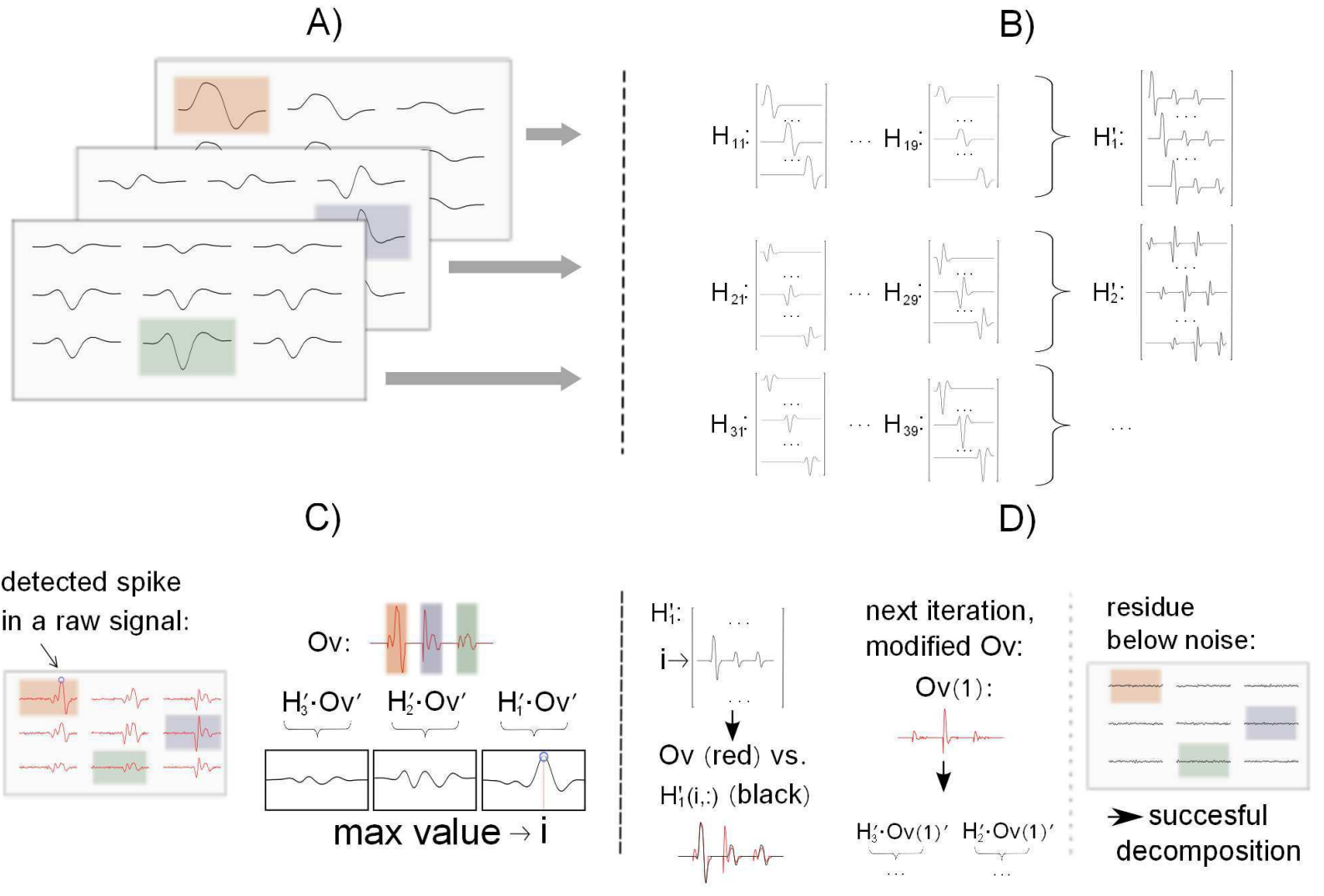


Figure 5
Click here to download Figure: Fig5.eps

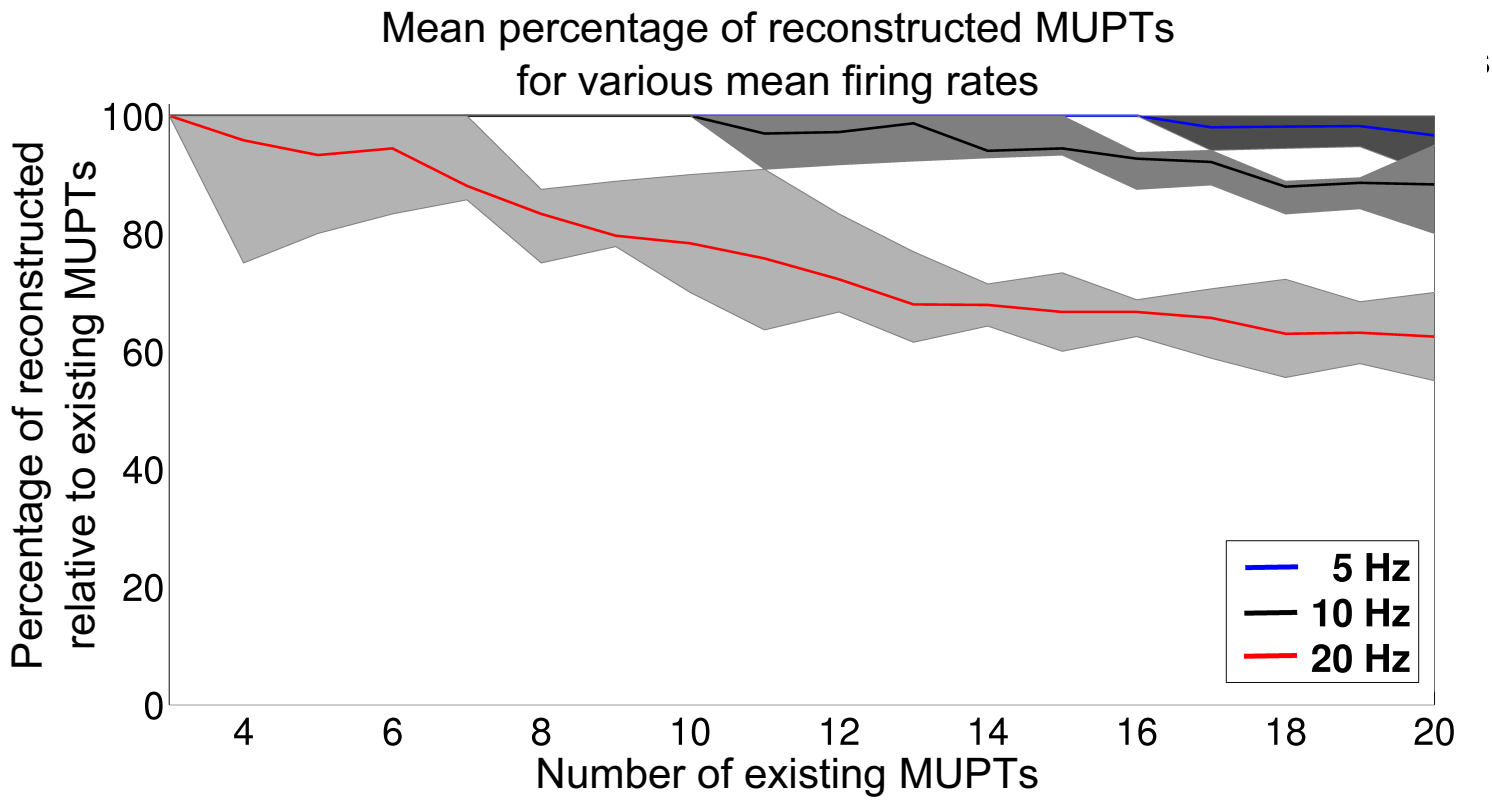


Figure 6
Click here to download Figure: Fig6.eps

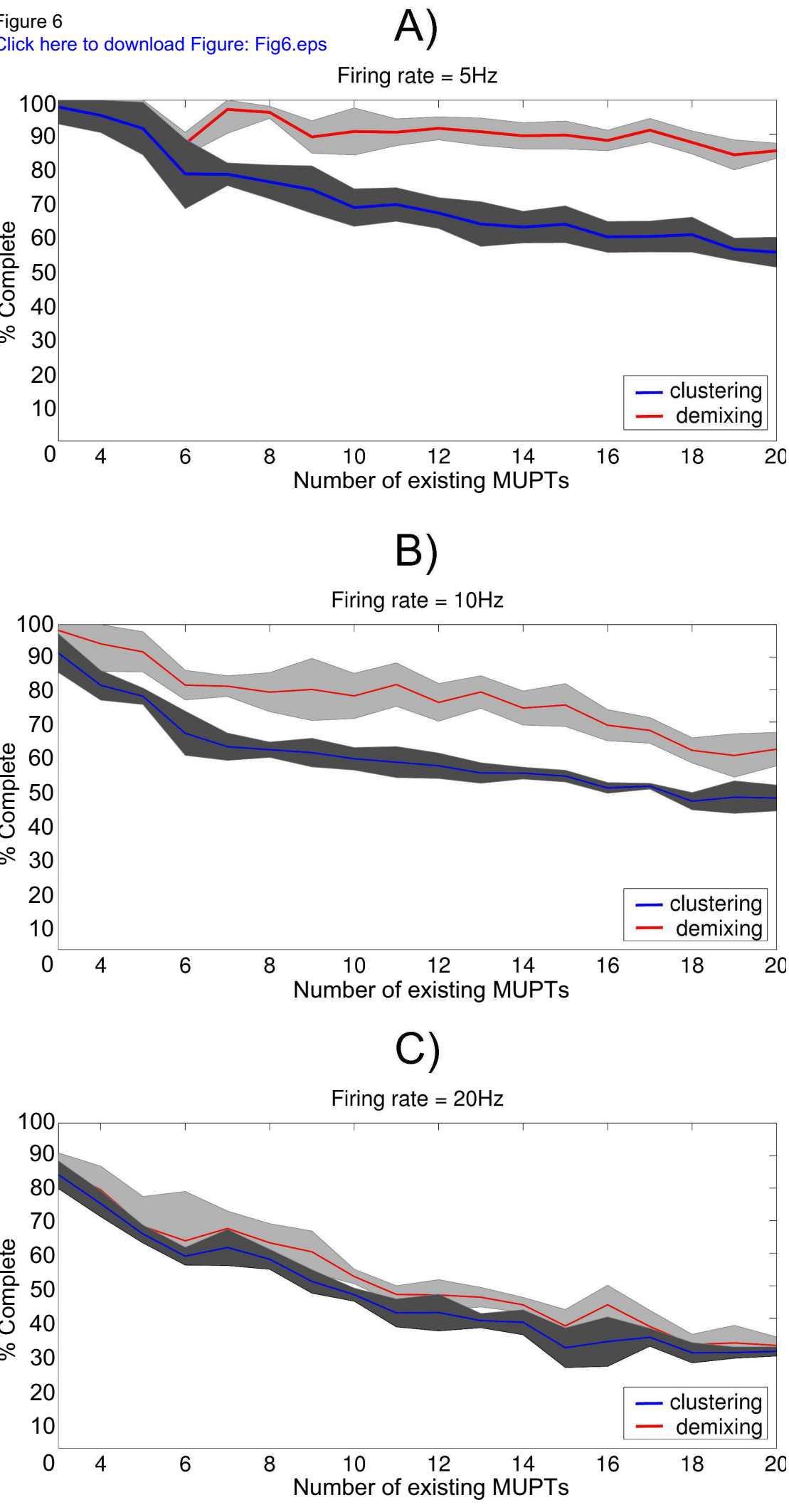


Figure 7
Click here to download Figure: Fig7.eps

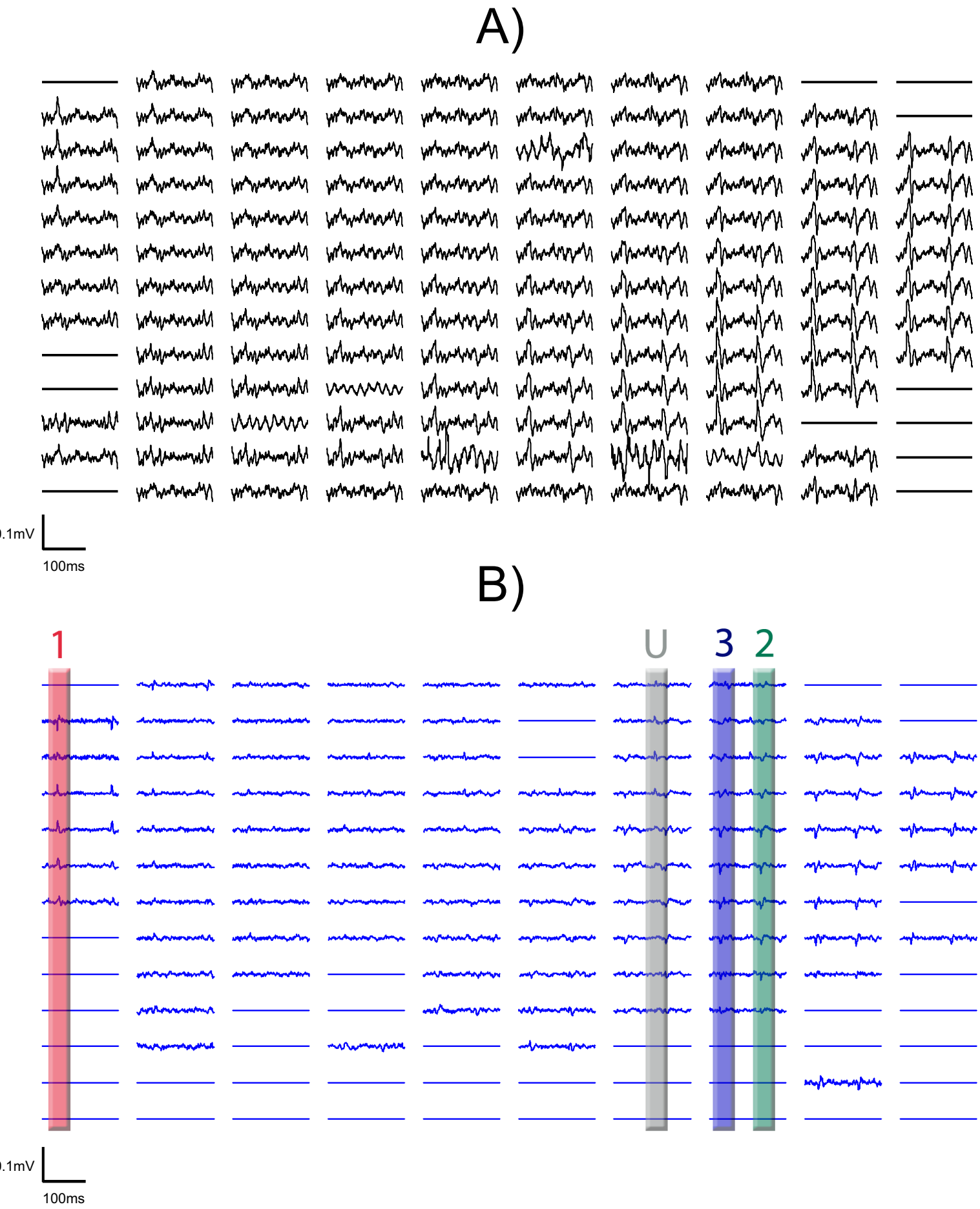


Figure 8
Click here to download Figure: Fig8.eps

